Journal of Applied Physics

RESEARCH ARTICLE | AUGUST 22 2023

Temperature dependence of resistivity of carbon micro/nanostructures: Microscale spatial distribution with mixed metallic and semiconductive behaviors FREE

Amin Karamati ; Cheng Deng ; Wangda Qu; Xianglan Bai ; Shen Xu ; Gyula Eres ; Xinwei Wang

Journal of Applied Physics 134, 085102 (2023)
https://doi.org/10.1063/5.0157932

AIP Publishing

Journal of Applied Physics ARTICLE pubs.aip.org/aip/jap

Temperature dependence of resistivity of carbon micro/nanostructures: Microscale spatial distribution with mixed metallic and semiconductive behaviors

Cite as: J. Appl. Phys. **134**, 085102 (2023); doi: 10.1063/5.0157932
Submitted: 12 May 2023 · Accepted: 2 August 2023 ·
Published Online: 22 August 2023

Amin Karamati,[1] Cheng Deng,[2] Wangda Qu,[3] Xianglan Bai,[1] Shen Xu,[4,b)] Gyula Eres,[5,b)] and Xinwei Wang[1,b)]

AFFILIATIONS

[1]Department of Mechanical Engineering, 271 Applied Science Complex II, Iowa State University, Ames, Iowa 50011, USA
[2]College of Mechatronics Engineering, Guangdong Polytechnic Normal University, Guangzhou 510635, People's Republic of China
[3]Laboratory of Lignin-based Materials, College of Life Sciences, Qingdao Agricultural University, Qingdao 266109, People's Republic of China
[4]School of Mechanical and Automotive Engineering, Shanghai University of Engineering Science, Shanghai, 201620, People's Republic of China
[5]Oak Ridge National Laboratory, Materials Science and Technology Division, Bldg. 4100, MS 6118, Oak Ridge, Tennessee 37831, USA

[b)]**Authors to whom correspondence should be addressed:** shxu16@sues.edu.cn; eresg@ornl.gov; and xwang3@iastate.edu

ABSTRACT

The temperature coefficient of resistivity (θ_T) of carbon-based materials is a critical property that directly determines their electrical response upon thermal impulses. It could have metal- (positive) or semiconductor-like (negative) behavior, depending on the combined temperature dependence of electron density and electron scattering. Its distribution in space is very difficult to measure and is rarely studied. Here, for the first time, we report that carbon-based micro/nanoscale structures have a strong non-uniform spatial distribution of θ_T. This distribution is probed by measuring the transient electro-thermal response of the material under extremely localized step laser heating and scanning, which magnifies the local θ_T effect in the measured transient voltage evolution. For carbon microfibers (CMFs), after electrical current annealing, θ_T varies from negative to positive from the sample end to the center with a magnitude change of >130% over <1 mm. This θ_T sign change is confirmed by directly testing smaller segments from different regions of an annealed CMF. For micro-thick carbon nanotube bundles, θ_T is found to have a relative change of >125% within a length of ~2 mm, uncovering strong metallic to semiconductive behavior change in space. Our θ_T scanning technique can be readily extended to nm-thick samples with μm scanning resolution to explore the distribution of θ_T and provide a deep insight into the local electron conduction.

I. INTRODUCTION

Carbon-based fibers have proved to have good electrical conductivity, high strength, and excellent electrochemical properties.[1] Considering the mentioned properties along with their lightweight, they have been used in different applications, from electrochemical energy storage, adsorption, batteries, and composite materials to phase change materials.[2–8] It is essential to know the properties of these fibers, such as thermal conductivity (k) and electrical resistivity.[8,9] The electrical resistance of carbon micro/nanostructures could have positive (metallic) or negative (semiconductive) temperature dependence, depending on the combined dependence of electron density and electron scattering.[10–12] Also, this dependence can

change from positive to negative with reduced temperature.[13] In some cases, the temperature dependence of electrical resistivity might vary strongly in space, but such variation is very hard to measure. This work reports the first-time mapping of the variation of temperature coefficient of resistivity ($\theta_T = d\rho_e/dT$, ρ_e: electrical resistivity) in space under localized laser heating and scanning. In the past, very rare work has been conducted on θ_T mapping. Instead, most works are focused on thermal and electrical conductivities' spatial mapping of different materials. For the mapping of thermophysical properties (mostly k), various techniques have been developed using the time-domain thermoreflectance technique (TDTR),[14–16] the frequency domain thermoreflectance (FDTR),[17] and the atomic force microscope-based methods.[18,19] For electrical properties mapping (mostly conductivity), terahertz time-domain spectroscopy (THz-TDS),[20] dry laser lithography (DLL), and micro four-point probes (M4PP) techniques,[21,22] electrical resistance tomography (ERT),[23,24] and electrical impedance tomography (EIT)[25,26] have been reported.

To date, θ_T has rarely been mapped. θ_T can be either positive (metal-like) or negative (semiconductor-like) for carbon structures. Yet, such θ_T sign spatial mapping is very challenging using current techniques and has not been reported to our best knowledge. In this study, we develop a new technique based on the scanning Transient Photo-Electro-Thermal (TPET) technique to probe a material's transient electro-thermal response under extremely localized laser heating. The obtained effective thermal diffusivity (α_{eff}) and its variation in space then allow us to extract θ_T pattern along the axial direction of the 1D microscale structure. To this end, both microscale carbon fibers and carbon nanotube (CNT) bundles are studied for such mapping capacity.

II. THERMAL DIFFUSIVITY MAPPING OF CARBON MICROFIBERS

A. Physics of scanning TPET

In this study, the TPET technique, as a proven method for high-sensitivity measurement of thermal diffusivity of 1D structures,[27,28] is adopted to measure the effective thermal diffusivity of our samples. This property directly carries the information about electrical resistivity's temperature dependence. Its schematic is depicted in Fig. 1(a). Implementing this technique, which was first developed in our laboratory,[29] requires the sample to be irradiated by an amplitude-modulated continuous wave (CW) laser beam serving as the heating source. Due to the temperature difference between the heating point and the sample, one-dimensional heat conduction starts as soon as the laser starts irradiating the sample. Additionally, the sample resistance changes as its temperature increases.

It should be noted that an absolute temperature rise is not needed here. Instead, its relative variation with time provides sufficient information to extract effective thermal diffusivity. To probe the small resistance change during the experiment, a small DC is passed through the sample, which produces a small voltage change to be recorded. This transient voltage change is used for extracting the thermal diffusivity. The transient voltage has an increasing trend if the sample's θ_T is positive or a decreasing one if θ_T is negative.[27] The transient temperature behavior of wires of a high length-to-diameter ratio is obtained by solving the heat transfer governing equation for 1D wire. The normalized average temperature rise of the sample is then expressed as[29]

$$T^* = \frac{96}{\pi^4}\sum_{m=1}^{\infty}\frac{1-\exp[-(2m-1)^2\pi^2\alpha t/L^2]}{(2m-1)^4}. \quad (1)$$

Here, T^* is the dimensionless temperature rise that has been normalized to the steady-state temperature rise, α is the thermal diffusivity, and L is the sample length. Equation (1) represents a solution for the case in which the sample is irradiated with a laser beam that covers the entire length of the sample. If the laser beam with a width of l is focused locally at position "ξ," the dimensionless temperature rise is given by[28]

$$T^* = \frac{1}{Z}\sum_{m=1}^{\infty}\left\{\frac{\cos[(2m-1)\pi\xi/L]-\cos[(2m-1)\pi(\xi+l)/L]}{(2m-1)^4}\times[1-\exp(-(2m-1)^2\pi^2\alpha t/L^2)]\right\}, \quad (2)$$

where

$$Z = \sum_{m=1}^{\infty}\left\{\frac{\cos[(2m-1)\pi\xi/L]-\cos[(2m-1)\pi(\xi+l)/L]}{(2m-1)^4}\right\}. \quad (3)$$

As explained in our previous work,[28] establishing a connection between the dimensionless temperature rise and the voltage data taken from the TPET experiment is done as

$$T^* = (V_0 - V)/(V_0 - V_1), \quad (4)$$

we will have

$$\ln|V - V_1| = -\pi^2\alpha t/L^2 + D, \quad (5)$$

where V_1 is the steady-state voltage and V_0 is the voltage at the beginning of the step of laser heating. It should be noted that the above relation has high accuracy when T^* is larger than 0.1 with consideration of experimental noise. Our data processing is conducted for a T^* range of $0.1 - 0.8$.[28]

Equation (5) indicates that performing a fitting between $\ln|V - V_1|$ and t provides the value of α for the sample. This fitting process is done for each location at which the sample is

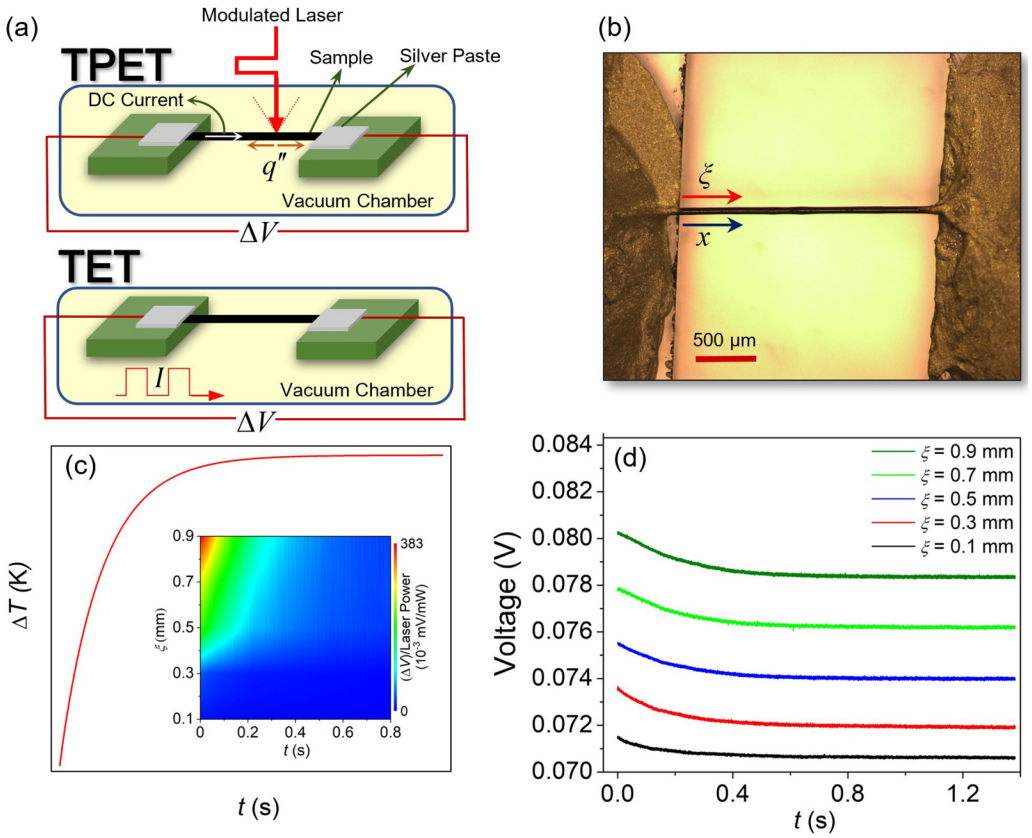

FIG. 1. (a) The schematics of TPET and TET techniques. (b) Optical image of the suspended carbon microfiber of 2.028 mm length. (c) Temperature evolution with time during the TET and TPET measurements. The inset is the ΔV/laser power ratio with time for half of the sample (CF) from the left end to the center during TPET scanning. (d) Voltage drop with time for different laser heating locations of the CF during TPET measurements under the same laser power irradiation (~6 mW).

irradiated to obtain the variation of α along the sample. This information is critical to the physical properties mapping as the measured voltage change is determined by θ_T, volumetric specific heat (ρc_p) and k, and their distribution in space. Since typical samples have non-uniform structures and properties along their length, the measured α in this work is an effective value, referred to as effective thermal diffusivity α_{eff}.

B. Experimental details for effective thermal diffusivity scanning of carbon microfibers

Pyrolytic lignin (PL) is utilized to produce the carbon microfibers (CMFs) studied in this work, and details about the sample synthesis can be found in the work by Qu *et al.*[30] The suspended carbon fiber (CF) is shown in Fig. 1(b). The length of the CF is measured to be 2.028 mm and its diameter is 55.2 μm. The resistance of the sample is measured to be 109 Ω. Silver paste is applied to secure the connection between the sample ends and electrodes, through which the output voltage is collected via an oscilloscope (Tektronix DPO3052). More details regarding the sample preparation can be found in the supplementary material. For running the TPET, a DC of 1.28 mA is fed through the sample to monitor the voltage variation during the test. This current value is chosen such that the voltage change is measurable, but the resulting Joule heating is not too high to alter the structure of the fiber. The whole test sample is then placed inside a vacuum chamber to run the TPET under less than 2 mTorr to make the convection effect negligible. To irradiate the sample locally, the laser spot is reshaped to a line of 0.1 mm width by a cylindrical lens. A 532 nm laser (DPSS) coupled with a modulator is used to heat the sample. The modulator is used to produce a square-shaped laser beam with a frequency of 0.2 Hz. As schematically shown in Fig. 1(c), the temperature of the sample rises with time upon laser irradiation. For a negative θ_T, the corresponding voltage change trend is downward, which is illustrated in Fig. 1(d). It is evident in Fig. 1(d) is the voltage drops as the laser beam starts irradiating the sample, and it reaches a steady-state voltage (V_1) with time.

Additionally, different levels of laser power are needed to have roughly the same level of voltage drop for different locations upon laser irradiation. It ranges from ~65 mW at the sample ends to ~6 mW at the middle. This is because the total thermal resistance from the laser heating location to the electrodes is much higher

when the laser irradiates the middle point than when irradiating the sample ends. Therefore, the temperature rise will be lower if a laser of the same power irradiates the sample's ends. For having almost the same temperature rise (voltage drop), a higher laser power (heat) should be applied to the locations near the sample ends. The contour plot in the inset in Fig. 1(c) depicts the ΔV/laser power ratio for different locations and firmly demonstrates this phenomenon. The ratio ranges from $1.5-7\,\mu V\,mW^{-1}$ for $\xi = 0.1$ mm (near the end) to $17-381\,\mu V\,mW^{-1}$ for $\xi = 0.9$ mm (near the middle). Considering that the sample is symmetric with respect to the center, these results have been presented for $\xi = 0.1$ mm to $\xi = 0.9$ mm.

In our work, the CF sample is subject to annealing to improve its structure, followed by mapping by the TPET technique for determining the material's property change in space. Annealing, as a treatment that produces a sample temperature increase, modifies the material's microstructure.[10,31] Liu *et al.*[10] showed that an increase is observed in CF's effective phonon and electron mean free path after annealing, resulting in an improvement in grain size and, consequently, fewer defects. To conduct the annealing, our sample is placed inside a vacuum chamber (<2 mTorr), and a DC as the heating source is applied to the sample. In what follows, we refer to the annealing processes as the first, second, and third annealing steps. Moreover, the transient electro-thermal (TET) technique is also used to measure the α_{eff} of the samples. The TET technique first developed by our lab in 2007[32] is also known as a reliable method to characterize micro/nanoscale wires.[33–38] As shown in Fig. 1(a), a step DC is passed through the sample in this measurement. The transient behavior of the voltage change (proportional to temperature change) induced by Joule heating is used to determine the sample's thermal diffusivity. The reason for using the transient voltage in the TET technique to determine α_{eff} instead of directly measuring k_{eff} is the larger uncertainties in k_{eff} measurement. To elaborate more on it, k_{eff} can be expressed as $I^2RL/12A_c\Delta T$[35] with ΔT as the steady state temperature rise. Not for all cases, A_c as the cross-sectional area might vary through the length of the sample. If the sample does not have a round cross section, precise determination of A_c becomes difficult. ΔT can be obtained as $\Delta R/(dR/dT)$, where the dR/dT is acquired by fitting R-T dataset in a separate calibration measurement. Again, this fitting will highly likely carry large uncertainties based on our experience. It should be noted that Eq. (1) is applicable to the TET technique in the same way as to the TPET. In our measurement, the thermal contact resistance between the supported part of the sample and the electrode is negligible. Detailed analysis is provided in the supplementary material.

C. Non-uniform α_{eff} of carbon microfibers under different laser heating locations

Details of the above annealing processes are presented in Table I. The magnitudes of the DC and the annealing time are chosen based on our group's previous work.[10] Also, this work has provided a detailed temperature rise study and structure characterization after annealing. Based on Table I, after the current annealing, the resistance of the sample decreases. The more the current value, the lower the resistance would be after annealing. This is because annealing improves the structure and it significantly increases the effective phonon mean free path. The effects of annealing on carbon microfibers' structure, electrical resistance, and thermal properties have been thoroughly investigated in our group's past work.[10] Figure 2(a) shows the TET measurements as well as the α_{eff} values for the original sample and its annealed versions. It is evident that after the annealing, the effective thermal diffusivity increases with the annealing current, changing from $1.32\times10^{-6}\,m^2\,s^{-1}$ at the original state to $2.32\times10^{-6}\,m^2\,s^{-1}$ at the end of the third annealing step. Therefore, a heat conduction capability improvement is observed for the CF that is attributed to defect reduction and structure enhancement. Comparing α_{eff} values measured using the TET and the TPET scanning method in Fig. 2(b) shows that the thermal diffusivity of each state's corresponding TET is very close to that of the TPET when the laser beam irradiates the central location.

TABLE I. Details of the annealing process for the CF sample.

Annealing process	DC value (mA)	Annealing time (s)	Resistance after the annealing (Ω)
First	50	70	76.2
Second	80	70	54.6
Third	100	70	42.7

The results of the TPET scanning are shown in Fig. 2(b). The left end of the sample is treated as the starting point of the coordinate for laser irradiation ($\xi = 0$ mm) as shown in Fig. 1(b). The α_{eff} for the heating locations near the edge (sample end) is higher than that for the middle zone, and it resembles a U-shaped pattern. This U-shaped pattern is not fully symmetrical for all states. In addition, the asymmetry changes from case to case. By comparing the annealing states, we also observe that generally, α_{eff} increases after annealing, and this increase is prevalent at both edges and the middle. From the original state to the third annealing, the largest difference in α_{eff} is observed between the locations near the edges and the middle point. From the center to the end, α_{eff} has changed by 58.5% for the original state, increasing to 68.9%, 76.8%, and 85.4% after the first, second, and third annealing, respectively. In our previous study,[28] we showed that the laser incidence location on the sample had a negligible effect on the calculated thermal diffusivity if the sample had uniform structure and properties along its length direction. To elaborate more, the key possible factors that can affect the fitted thermal diffusivity of a sample are its structure and the possible distribution of k, ρc_p, and θ_T. So, if the calculated thermal diffusivity does not remain constant based on different laser incident locations, it means all the structure and the properties (i.e., k, ρc_p, and θ_T) or at least the most contributing one change along the sample's length direction. However, TPET scanning of the original state (before annealing) deviates from the previous results and follows the U-shaped pattern characteristic for the annealed samples. A plausible explanation of this observation is that the current applied during the TET measurement before performing the TPET mapping produces weak annealing of the sample. Even this weak annealing will facilitate some grain boundary improvement and impurities removal to improve the overall structure.[10]

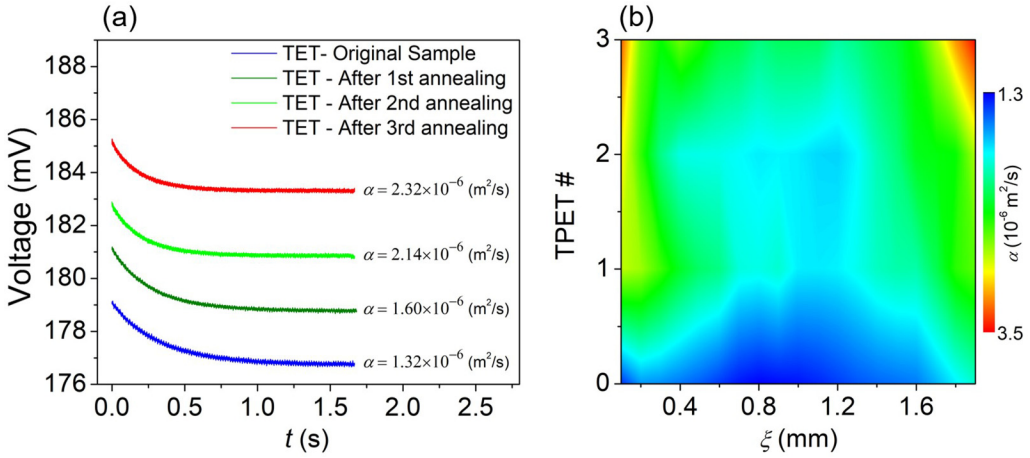

FIG. 2. (a) The CF TET signals (experimental data) and the corresponding thermal diffusivity values for the original sample and after different annealing steps. (b) Effective thermal diffusivity variation with laser heating location obtained via TPET technique for the original sample and after different annealing steps. TPET # 0, 1, 2, and 3 refer to the TPET measurement conducted for the original sample after the first, second, and third annealing, respectively.

As mentioned before, based on our recent study,[28] we confirmed that the laser heating location had a negligible effect on the distribution of the thermal diffusivity through the length of the sample, and the thermal diffusivity remained almost constant. However, scanning the annealed CF reveals that the fitted thermal diffusivity has a significant dependence on the laser heating location. The distribution of α_{eff} after the annealing steps shown in Fig. 2(b) prompts us to examine the factors contributing to these effects. A theoretical study is performed and described in Sec. II D to identify possible factors that can affect the α_{eff} distribution. Then, an investigation of the most effective factor(s) is conducted to map the experimental α_{eff} distribution.

D. Effect of k, ρc_p, and θ_T: A theoretical study

As discussed earlier, the relationship between the normalized temperature rise and the voltage taken from the experimental data reveals that the thermal diffusivity value obtained from fitting $\ln|V - V_1|$ with time carries information about the distribution of both k and ρc_p of the wire. Also, the voltage carries information about θ_T as $dV = \int \theta_T I \Delta T / A_c dx$, where ΔT is the local temperature rise. Therefore, the effects of these three parameters distribution on α_{eff} are studied in this section. In each case, the effect of every parameter is analyzed separately, with the others assumed to be uniform over the sample length. This is intended to provide a better understanding of every single physical property's effect on α_{eff} distribution in space. In Figs. 3(a)–3(c), it is assumed that only ρc_p, k, or θ_T changes linearly from the middle of the sample to its both ends. It should be noted that for each case, by changing ρc_p, k, or θ_T, other properties are treated constant over the entire sample length. The overall relative change varies in a range of −30% to +30%. Also, the values of the ρc_p, k, and θ_T at the central location take $1.552 \times 10^6\,\mathrm{J\,m^{-3}\,K^{-1}}$, $2.5\,\mathrm{W m^{-1} K^{-1}}$, and 1 a.u., respectively. Note that in this work, limited by the unknown temperature rise of the sample during TPET measurement, we only study the distribution of relative/normalized θ_T and not its absolute value. However, obtaining the relative θ_T with its sign still provides an excellent understanding of the structure uniformity and helps understand the local electron conduction mechanism. The governing heat conduction equation can be expressed as

$$\frac{\partial(T\rho c_p)}{\partial t} = \frac{\partial}{\partial x}\left(k\frac{\partial T}{\partial x}\right) + \dot{q}(x,t), \tag{6}$$

where both k and ρc_p are allowed to vary in space. Also, the heating source ($\dot{q}$) takes the location and size of the focused laser line in the modeling. For this study, 1D numerical modeling is conducted to solve the heat conduction along the sample under localized laser heating with full consideration of the property distribution in space. The modeling is based on the finite volume method with the implicit algorithm. The time step takes 0.25 ms and the mesh size is 1 μm. Also, the TDMA (TriDiagonal Matrix Algorithm) method is used to solve the equations. Moreover, the modeled voltage change (response) is calculated considering each point's temperature rise and the local θ_T, which is then fitted using Eq. (5) to determine α_{eff}. It should be noted that in this modeling, the absolute temperature rise is not critical and is not needed. Only an arbitrary heating (not too high to can result in a considerable radiation effect) is used to irradiate the sample.

Figures 3(a) and 3(b) show that the linear change of ρc_p and k brings about a specific variation of α_{eff} through the sample. However, the range of the α_{eff} change is not as large as that of the actual physical property under study. The maximum change of α_{eff} over space is only 3.4% and 3.5% for the non-uniform ρc_p and k cases, respectively. Figure 3(c) shows that a −30% to +30% linear change in θ_T from the middle of the sample to its both ends corresponds to about 3.8% change in the distribution of α_{eff}. Note that changes much larger than 30% in physical properties do not cause a considerable change in α_{eff} distribution range through the sample.

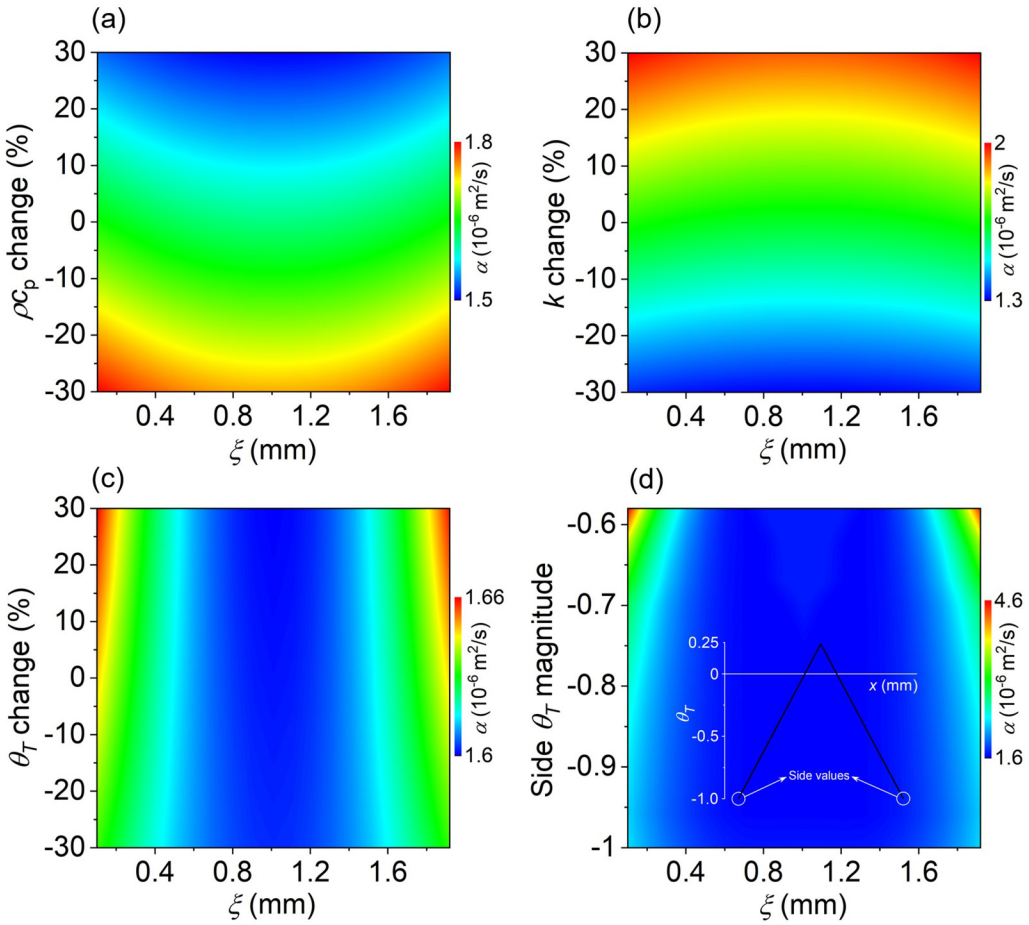

FIG. 3. Effective thermal diffusivity variation with location for −30% to +30% linear change of (a) volumetric specific heat, (b) thermal conductivity, and (c) temperature coefficient of electrical resistance (θ_T) from the center of the CF to its both ends. (d) Effective thermal diffusivity variation with location for a specific pattern of θ_T shown as the inset.

For instance, with a 100% linear increase for ρc_p, k, and θ_T from the middle of the sample to its ends, the range of the α_{eff} change is only 1.7%, 4.5%, and 5.4%, respectively. However, large changes in these properties cause the thermal diffusivity distribution to deviate from the U-shaped pattern observed in our experiments.

To reproduce the characteristic change in α_{eff} through the sample, a unique θ_T distribution pattern is needed. Among all the parameters under, only θ_T can be both positive and negative along the sample. We assumed a hypothetical distribution to be negative at both ends, and it linearly increases toward the middle of the sample, where it becomes positive. This distribution is illustrated in the inset in Fig. 3(d). The effect of the θ_T magnitude change on the thermal diffusivity distribution at the sample ends, termed "side θ_T magnitude," is investigated next. The magnitude of θ_T at the sample ends is varied between (−1) and (−0.58), while the middle point θ_T takes a constant of +0.25. Figure 3(d) shows not only a clear distribution of thermal diffusivity along the sample length, but it demonstrates a substantial variation in α_{eff} between the ends and the middle regions. This change of the side θ_T value (i.e., −0.58 to −1), results in 187% difference between the maximum and minimum of α_{eff}. Consequently, this finding prompts the θ_T distribution as the key factor affecting the α_{eff} distribution that is explored in Sec. II E.

E. Probing sign change of θ_T based on α_{eff} mapping

Up to this point, thermal characterization of CF before and after annealing has been conducted, and the properties and the extent to which they can affect the distribution of α_{eff} have been investigated. In this section, we attempt to determine the relationship between the distribution of α_{eff} and θ_T for the annealed CF and to probe θ_T distribution to fit the α_{eff} distribution. As discussed in Sec. II D, the θ_T distribution with negative values near the sample ends and positive values near the middle corresponds to the largest variation in the α_{eff} distribution. Therefore, considering such a distribution of θ_T, a one-dimensional modeling is

conducted by developing a code for high-fidelity temperature modeling and overall relative voltage variation with time. This procedure is conducted to find the θ_T distribution that leads to the numerical α_{eff} distribution giving the best fit of the experimental results.

The ρc_p and k in our modeling and fitting are considered to be fixed along the sample length as they do not affect the α_{eff} distribution much. To this end, ρc_p of graphite (1.552×10^6 J m^{-3} K^{-1}) is used for the CF, and the k value is calculated as $k = \rho c_p \alpha_{eff}$ after each annealing case, where α_{eff} is the effective thermal diffusivity measured using the TET technique. This treatment can be justified by one important observation of the numerical results shown in Fig. 3. It is found that the α_{eff} when the laser irradiates the sample's middle point is very close to the α_{eff} measured using the TET method regardless of the properties variation in space. This is also observed in the experimental results shown in Fig. 4. Also, this α_{eff} value is very close to the average thermal diffusivity of the sample if the sample's k or ρc_p varies in space. For instance, when k increases by 30% from the middle to the end, its average thermal diffusivity (calculated using the spatially averaged thermal conductivity) is 1.85×10^{-6} m^2 s^{-1}. Our modeling shows the TET technique will give an α_{eff} of 1.94×10^{-6} m^2 s^{-1}, and the TPET will give an α_{eff} of 1.93×10^{-6} m^2 s^{-1} when the laser irradiates the middle point. For the case study in Fig. 3(d), the middle point α_{eff} is always 1.59×10^{-6} m^2 s^{-1}, regardless of the side θ_T magnitude, very close to the real thermal diffusivity of the sample, which is 1.61×10^{-6} m^2 s^{-1}. When the side θ_T magnitude is -1.0, our modeling shows that TET will give a α_{eff} of 1.65×10^{-6} m^2 s^{-1}, very close to the sample's real thermal diffusivity.

Figures 4(b)–4(d) show the experimental results for α_{eff} variation in space after each annealing treatment along with the fitted values taken from the numerical simulation. Using the same finite volume based numerical modeling discussed before, and the θ_T distribution in space, the α_{eff} is calculated for each laser heating location, which are then compared with the experimental α_{eff} distribution. Later on, the same process will be used for the CNT samples in this work. Based on Fig. 4(b), α_{eff} at the beginning of

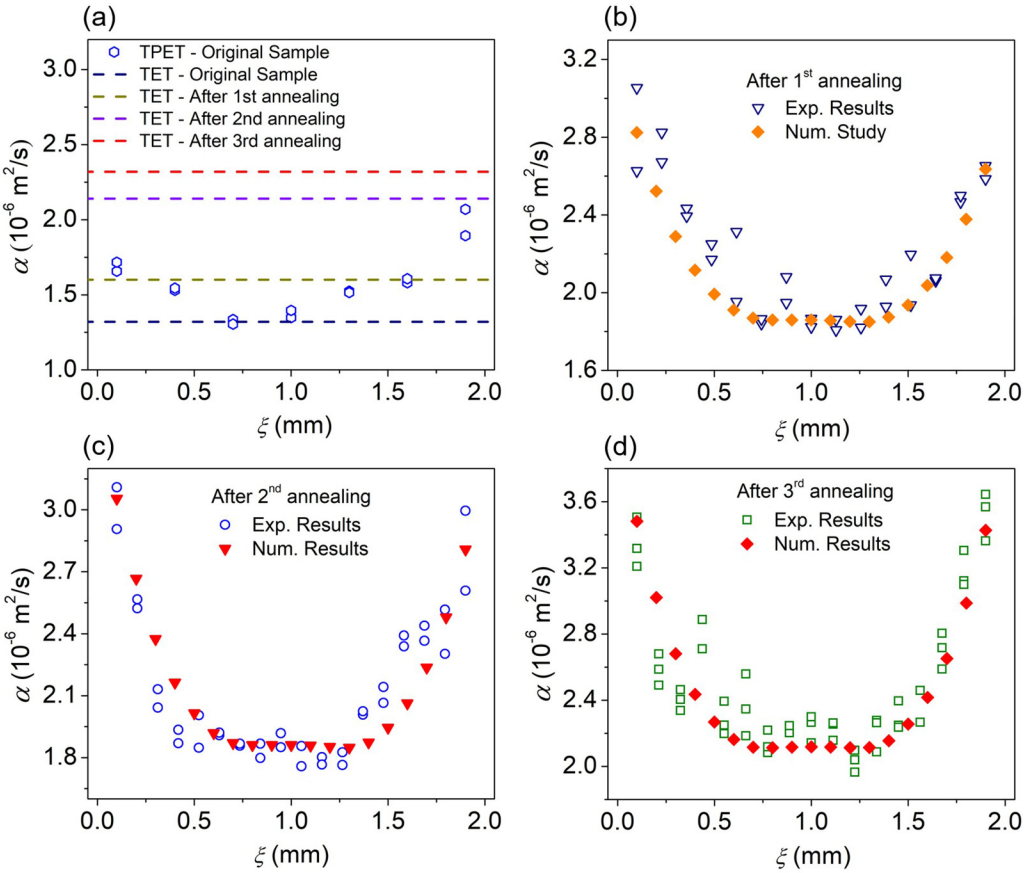

FIG. 4. (a) Effective thermal diffusivity distribution with the laser heating location for the original CF. The TET results for the original CF, after the first, second, and third annealing, have been presented as dashed lines. Effective thermal diffusivity values for different laser heating locations obtained via the TPET technique along with the results from the numerical mapping simulation considering a particular distribution of θ_T: (b) after first annealing, (c) after second annealing, (d) after third annealing.

TABLE II. Summary of the CF θ_T variance considering the combination of different factors.

	θ_T		ΔV/Laser power (μV/mW)		t_c (s)	
Annealing step	$x = 1.0$ mm (middle)	$x = 2.028$ mm (edge)	$x = 1.0$ mm (middle)	$x = 2.028$ mm (edge)	$x = 1.0$ mm (middle)	$x = 2.028$ mm (edge)
First	+0.28	−0.95	320	21.2	0.43	0.48
Second	+0.31	−0.95	244.2	7.35	0.59	0.51
Third	+0.33	−1	272	11.7	0.45	0.43

the sample is slightly higher than that of the ending tail. Therefore, the two ends of the sample should have slightly different θ_T. In our modeling, it is assumed that θ_T has a linear distribution between the ends and the middle point. Before annealing, our TET measurement showed a resistance decrease upon heating, so we fix θ_T at the sample beginning ($x = 0$ mm) to be a reference value of −1. Examining different combinations for the middle and the end θ_T values [following the pattern shown as the inset in Fig. 3(d)] is done to fit the α_{eff} values after the first annealing. The best result is obtained for values of +0.28 and −0.95 for $x = 1.0$ mm (middle) and $x = 2.028$ mm (end), respectively. Performing the fitting of the experimental data after the second and third annealing, the corresponding θ_T values for the middle ($x = 1.0$ mm) and end ($x = 2.028$ mm) of the sample are determined to be (+0.31, −0.95) and (+0.33, −1) for the two cases, respectively. It is observed that the values of θ_T for both ends of the sample are very close to each other, as the annealing has the least effect on sample ends. This is because of being in the vicinity of constant temperature electrodes, and consequently, their temperature change during the annealing is very low. Apart from that, an overall increase in the middle location's θ_T value is observed by increasing the current from the first annealing to the third one, hence causing a bigger variation in the corresponding α_{eff} distribution. In Sec. III, we experimentally validate the θ_T sign change (negative at the sample ends and positive in the middle) we have discovered to this point. A summary of the θ_T change for each combination of x (e.g., middle and edge), ΔV, and t_c is presented in Table II. t_c is the characteristic time at which the normalized temperature given in Eq. (2) reaches 0.8665.

III. EXPERIMENTAL VALIDATION OF THE θ_T SIGN CHANGE IN SPACE

In this section, we validate the finding uncovered by the TPET scanning, which shows that θ_T changes the sign from the sample ends (negative) to the middle (positive). Such change is caused by structure variation of the sample along its length. Scanning Raman spectroscopy is performed after each annealing process for the samples studied above. Figure 5(a) shows that carbon materials' two prominent D and G characteristics are present in the Raman spectra after the third annealing. Moreover, the D and G peaks have more overlap around the edge of the sample ($x = 2.028$ mm), and they become sharper and more separated around the center of the sample ($x = 1.0$ mm). All these indicate the structure improvement from the middle to the ends of the sample. Figure 5(b) also shows that the D and G peaks linewidth broadens from the center to the edges, which is again an indicator of the structural improvement in the central region by annealing.

To further investigate the effects of annealing on θ_T, a CF of ∼5 mm length is suspended and placed in vacuum, and a DC of 100 mA (equal to the current used for the third annealing) is run through the sample for 70 s. Figure 5(c) shows the schematic temperature distribution that arises through the sample, with a maximum in its middle part. To confirm the veracity of the hypothesis for the θ_T distribution we described above, two small segments are cut from the middle ($L_m = 1.054$ mm) and the ends ($L_s = 1.581$ mm) of the annealed ∼5 mm long CF sample. They are suspended and tested by under step DC heating to check their resistance change under heating. Interestingly, based on voltage signals shown in Fig. 5(d), the transient voltage for the middle segment is increasing, corresponding to a positive θ_T. For the end segment, however, the voltage is decreasing, indicating a negative θ_T. This critical finding exactly proves the discovery made from the θ_T sign probing based on the α_{eff} distribution. We note that investigation of different samples for whether θ_T can be positive or negative has also been conducted by our group in the past. CNTs, for instance, were shown to have negative θ_T at their original state.[27,39] Based on another two studies,[40,41] graphene foams tended to have positive θ_T. Carbon fibers, as another type of sample, were shown to have negative θ_T before and after the annealing process at different temperatures.[10,42] For the graphene paper, however, Xie *et al.*[13] showed that the TET signal changes from a clear voltage rise to a voltage drop pattern as the environmental temperature decreases, which indicated a positive-to-negative transition in θ_T for the sample.

The Raman measurements for this sample are conducted with a 20× objective and a laser power of ∼9 mW. Using this objective, the laser spot size on the sample is ∼1.4 μm. So, it heats a very small portion of the sample. The heating would swiftly dissipate through the sample and will cause a negligible structure change. Also, the laser power in Raman characterization is far lower than the power produced (∼190–430 mW) in the annealing process through the whole sample via electrical current.

To qualitatively explain the physics of the observed θ_T distribution, we analyze the electrical resistivity (ρ_e) expressed by

$$\rho_e = \frac{m}{ne^2\tau}, \tag{7}$$

where m is the electron mass, n is the volumetric number density of conduction electrons, and τ is the characteristic collision time.[43] Therefore, θ_T (i.e., $d\rho_e/dT$) is a function of both dn/dT and $d\tau/dT$.

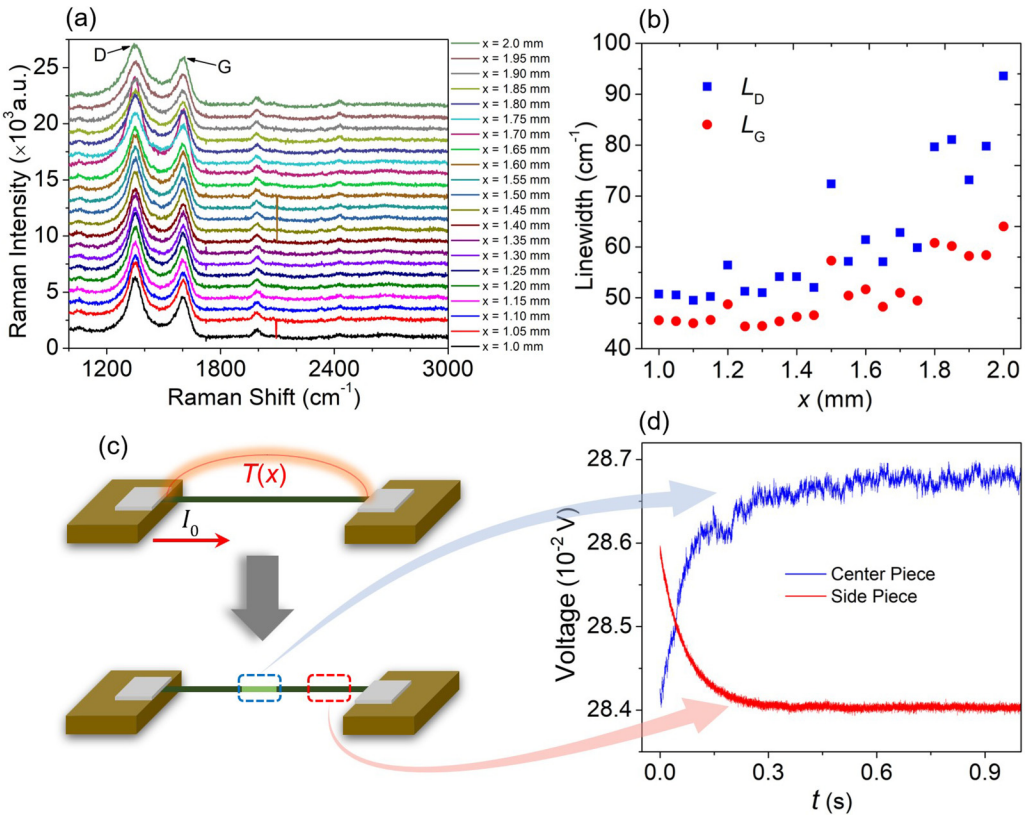

FIG. 5. (a) Raman spectra at different locations of the CF after the third annealing. (b) The D and G peaks linewidth at different locations of the CF after the third annealing. (c) A schematic of the suspended ~ 5 mm long CF used for experimental validation of the spatial θ_T distribution obtained by thermal diffusivity mapping. (d) The TET signals for the central and side segments of the annealed ~ 5 mm long CF. (Note: The TET signal for the side segment has been given an offset to show it in one graph.)

Annealing, which leads to a temperature increase in the sample, improves the structure of the sample by reducing impurity concentration, thereby increasing the conduction electron population n. On the other hand, electron collisions mainly happen due to structural defects in our samples. The τ change is driven by two factors: scattering by the lattice vibrations termed "phonons" and scattering by imperfections and impurities.[44]

These scattering processes have different temperature dependencies. It can be affirmed that temperature has a weak effect on the scattering caused by defects. However, it has a stronger effect on the scattering induced by phonons as the phonon population increases with temperature. Consequently, the higher the temperature, the higher the phonons population, which leads to a decrease in characteristic collision time between electrons and phonons and, ultimately, a negative value for $d\tau/dT$. However, when temperature increases, the population of conduction electrons increases due to thermal excitation. So, the combined effect of the two terms of dn/dT and $d\tau/dT$ can vary in different regions of the sample, leading to θ_T distribution introduced in the CF's thermal diffusivity mapping. Qualitatively speaking, before annealing, the sample's electron scattering is mainly induced by defects, and this has weak temperature dependence. But ρ_e will be strongly affected by n (n increases with increased temperature due to thermal excitation). Therefore, θ_T would be negative. After annealing, the sample structure improves, and phonon-electron scattering becomes more important. When the temperature increases, this scattering becomes more intense, overtaking the effect of n. Therefore, θ_T becomes positive.

IV. PROBING OF θ_T SIGN VARIATION ALONG MICROSCALE CNT BUNDLE

Apart from CF, vertically aligned carbon nanotube (VACNT) bundles' characteristics are also investigated using TPET mapping. The chemical vapor deposition (CVD) technique is used to produce the VACNT bundles that are utilized in this study. In more detail, ferrocene [$Fe(C_5H_5)_2$] and a gas mixture of 2% C_2H_2, 10% H_2, and 88% He are added to a chamber that was previously filled with silicon wafers coated with catalytic metal layers (10 nm Al layers and 1 nm Fe layers), which ultimately results in the growth of CNTs at the end (base growth).[27] This section discusses the results of two CNT bundles on which the TET and TPET scanning are carried out. Characteristics of the CNT samples are presented in Table III. Based on the TET measurements, the

TABLE III. The CNT samples size and their α_{eff} obtained using the TET.

Sample #	Length (μm)	Width (μm)	α_{eff} ($m^2\,s^{-1}$)
1	2106	97.7	4.25×10^{-5}
2	2211	165.5	1.59×10^{-5}

effective thermal diffusivities of samples 1 and 2 are measured to be 4.25×10^{-5} and $1.59 \times 10^{-5} m^2 s^{-1}$, respectively. Then, TPET scanning is used to characterize the samples.

The α_{eff} variation with laser location on the sample is shown in Figs. 6(d) and 6(e). Noticeably, there is no consistent trend in α_{eff} variation with the location: having higher values near the two ends and the minimum at the center for sample 1 and an ever-increasing trend for sample 2 from one end to the other. So, these findings prompt us to delve deeper into the structure of the CNTs. Figure 6(a) depicts the CNT sample's optical image under 4× magnification. To have a better understanding of the CNTs' structural detail, their scanning electron microscope (SEM) images are also presented in Figs. 6(b) and 6(c), which have been taken under 150× and 5000× magnification, respectively. As can be seen in Figs. 6(a) and 6(b), the bundle seems to be well straight along its axis. However, under higher magnification [Fig. 6(c)], it is uncovered that along the direction of VACNTs' growth, different macroscopic nanotube assemblies' order, alignment, and inhomogeneity appear.[27] So, the CNT bundles' structure is not uniform, and the alignment of nanotubes along their axis is, in fact, poor, and they are tangled, and haphazard contact between single nanotubes is prevalent in different parts of CNTs. This explains the different α_{eff} distribution shown in Figs. 6(d) and 6(e).

Next, fitting of the TPET results for α_{eff} variation with the location is performed considering a distribution for the θ_T along the CNT's length. As shown in Fig. 6(d), the change in magnitude from one end to the other is very large. Based on the simulation results shown in Figs. 3(a)–3(d), this amount of change is caused neither by changes in k nor ρc_p. For CNT No. 1, the symmetrical θ_T distribution shown as the inset in Fig. 3(d) can cause the thermal diffusivity distribution along its length. However, for CNT No. 2, a nonsymmetrical form of θ_T distribution can be the reason for this sample's α_{eff} variation, which is shown as the inset in Fig. 6(e). Besides, using the specific heat of graphite ($\sim$710 $J\,kg^{-1}K^{-1}$) and considering the density of the bundle to be $\sim$316.9 $kg\,m^{-3}$,[45] the thermal conductivity of each CNT sample is calculated by $k = \rho c_p \alpha_{eff}$, where α_{eff} is the effective thermal diffusivity measured by the TET technique. Ultimately, adapting a reference value of -1 for the θ_T in the end of the sample ($x = 2.106$ mm) of sample 1, the best mapping result occurs using the θ_T values of $+0.25$ for the middle ($x = 1.05$ mm) and -0.91 for the beginning ($x = 0$ mm) of the sample, which has been shown in Fig. 6(d).

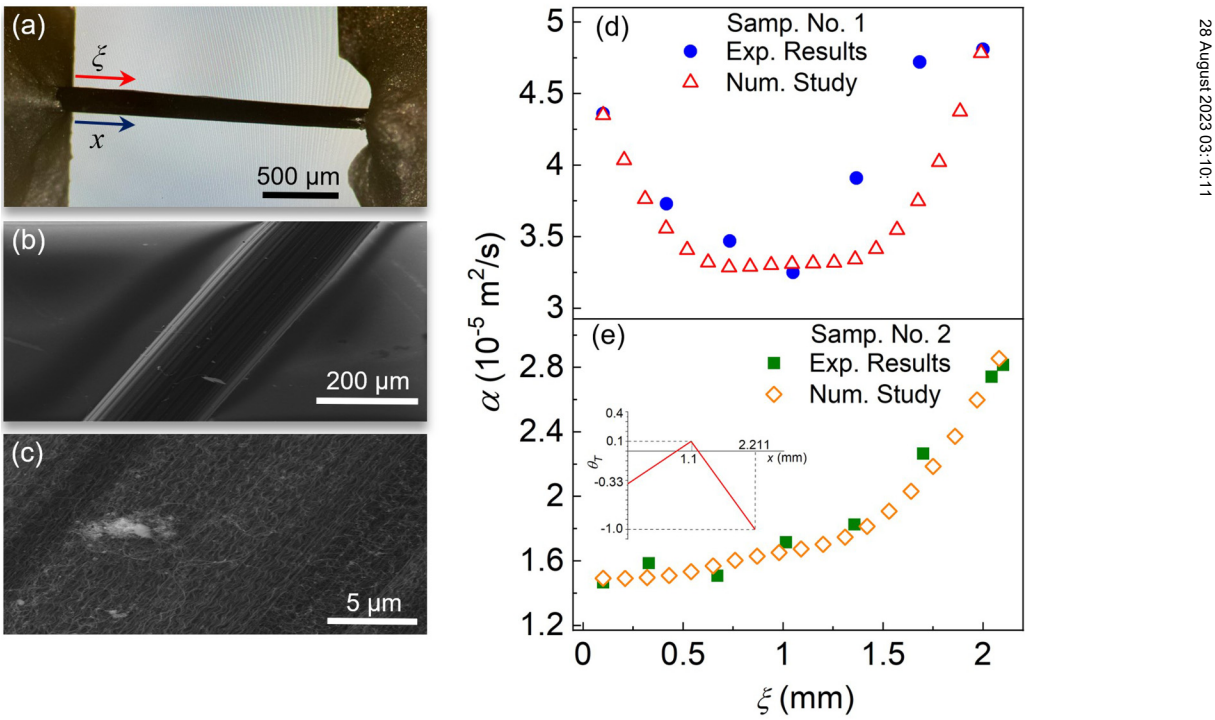

FIG. 6. (a) Optical image of the CNT sample. (b) and (c) are the SEM images of CNTs under 150× and 5000× magnifications, respectively. In (c), the individual straight and curly CNTs are clearly visible. (d) and (e) show the effective thermal diffusivity distributions for the experimental (TPET) and numerical simulation for CNT samples (No. 1 and No. 2). The inset in (e) depicts the special asymmetrical θ_T distribution causing the peculiar thermal diffusivity variation for CNT No. 2.

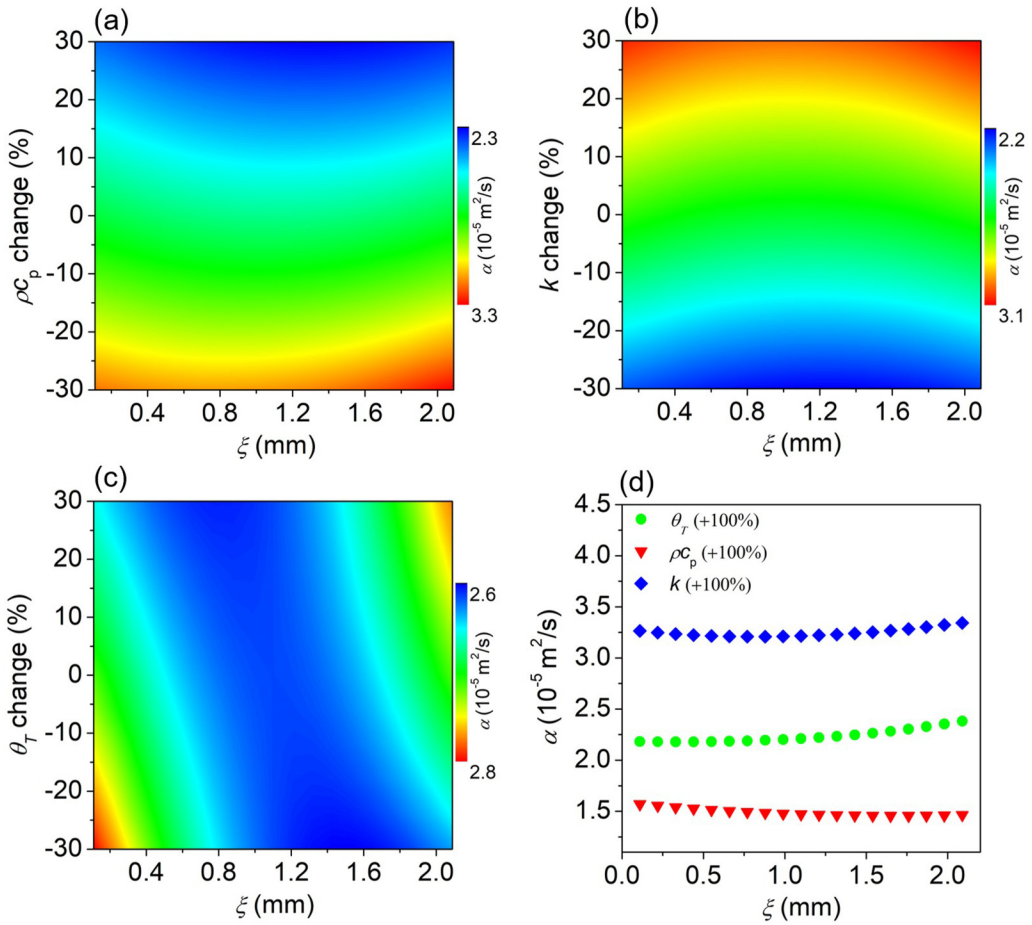

FIG. 7. Effective thermal diffusivity variation with location for −30% to +30% linear change of (a) volumetric specific heat, (b) thermal conductivity, and (c) temperature coefficient of electrical resistance (θ_T) from one end (root) to the other end (tip) of CNT. (d) Effective thermal diffusivity variation with location for extreme (+100%) linear changes in ρc_p, k, and θ_T of CNT from root to the tip region.

For sample 2, however, as it had an increasing tendency from left to right, and is totally different, other distributions, such as −30% to +30% linear change from one end (root) to the other end (tip) are double checked for ρc_p, k, and θ_T [Figs. 7(a)–7(c)], just in case they will produce an acceptable mapping. Still, they cannot match the experimental results. Additionally, extreme linear changes of about 100% are also examined for ρc_p, k, and θ_T [Fig. 7(d)], bringing about only 7.7%, 4.2%, and 9.3% in the thermal diffusivity variation. Moreover, the combinations of these extreme changes cannot cause a considerable variation in thermal diffusivity through the sample's length. So, again assuming the θ_T value to be a reference value of −1 at the end of the sample ($x = 2.211$ mm), the mapping is done for sample 2 using the θ_T values of (+0.1, −0.33) for the middle ($x = 1.1$ mm) and the beginning ($x = 0$ mm) of the sample. This significant result indicates how the combined effects of structure variation, alignment, and contact of CNTs have brought about such a large variation in θ_T along the length of the sample. It is speculated that the θ_T variation is more likely caused by the random contact among CNTs in the bundle since the electrical contact resistance plays an important role in the overall electrical resistance.

For the CNT bundles studied in this work, they have a strong variation of the structure and properties along the growing direction. The location of $\xi = 0$ mm is close to the root (close to the substrate), and the other end is the tip region (a region grown first). As detailed in our recent work,[27] the tip region has better alignment than the root region. Therefore, it is expected that the root region will have more CNT–CNT wall contacts. This could help qualitatively explain the variation of α_{eff} shown in Fig. 6(e) as it shows a monotonic variation trend against ξ. The quite symmetrical α_{eff} distribution and the mapped θ_T distribution for sample 1 shown in Fig. 6(d) could be caused by the weak annealing effect during our TET measurement. However, for sample 2, the random contact effect overshadows the weak annealing effect, leading to monotonic properties change along the x direction.

As uncovered by our numerical study, the k and ρc_p variations in space only cause a very small variation of α_{eff} in space. The measured thermal diffusivity by TET and TPET is very close to the average thermal diffusivity of the sample. If θ_T does not change sign in space, its variation will also cause a small variation of α_{eff} in space. However, the reported α_{eff} distribution will be strongly affected by sign variation of θ_T in space, namely, the change from metallic to semiconductive behavior. Therefore, this proposes a very effective way to probe the metallic and semiconductive behavior variation in space based on the α_{eff} distribution. So, the method can be applied to many 2D materials, like black phosphorus, MoS_2, etc., whose impurity and defect level could dramatically change the electron scattering behavior. Apart from that, the TPET scanning method can be utilized for even thinner micro/nanoscale samples to probe their θ_T sign based on the α_{eff} distribution as long as the laser beam can irradiate the sample effectively and locally.

V. CONCLUSION

We reported a study for characterizing the distribution of the relative temperature coefficient of resistivity (θ_T) of microscale CF and CNT bundles by evaluating the measured effective thermal diffusivity using scanning TPET. Three annealing steps were carried out on the CFs, creating a distribution of α_{eff} as a function of the laser heating location. Our study revealed that the change in ρc_p and k has a weak effect on the α_{eff} distribution. Rather the measured α_{eff} distribution prompted θ_T change from semiconductive (negative) to metallic (positive) behavior from the sample ends to the middle region. This finding was confirmed directly using an annealed CF sample, whose middle and end parts were tested separately under step DC heating. α_{eff} mapping of CNT bundles was also conducted using the TPET technique. The corresponding θ_T distribution was determined, and it showed metallic to semiconductive behavior variation in space, suggesting a strong effect of CNT–CNT wall contacts on electrical resistance and its temperature dependence. The method reported in this work can be readily applied to other micro/nanoscale materials to probe the θ_T sign change in space with microscale resolution.

SUPPLEMENTARY MATERIAL

See supplementary material for carbon microfiber preparation and suspension methods as well as the contact resistance evaluation in the presence of silver paste.

ACKNOWLEDGMENTS

This work was partially supported by the US National Science Foundation (Nos. CBET1930866 and CMMI2032464 for X.W.), Guangdong Basic and Applied Basic Research Foundation (No. 2023A1515012684 for C.D.), and National Natural Science Foundation of China (No. 52106220 for S.X.). The contribution by G.E. was supported by the Department of Energy (DOE), Office of Science, Basic Energy Sciences (BES), Materials Sciences and Engineering Division.

AUTHOR DECLARATIONS

Conflict of Interest

The authors declare that they have no known competing financial interests or personal relationships that could have appeared to influence the work reported in this paper.

Author Contributions

Amin Karamati: Data curation (equal); Formal analysis (equal); Investigation (equal); Writing – original draft (equal). **Cheng Deng:** Conceptualization (equal); Data curation (equal); Formal analysis (equal); Investigation (equal); Methodology (equal); Validation (equal); Writing – review & editing (equal). **Wangda Qu:** Data curation (supporting); Formal analysis (supporting); Investigation (supporting); Resources (supporting); Writing – review & editing (supporting). **Xianglan Bai:** Data curation (supporting); Investigation (supporting); Methodology (supporting); Writing – review & editing (supporting). **Shen Xu:** Conceptualization (equal); Data curation (equal); Methodology (equal); Resources (equal); Supervision (equal); Writing – review & editing (equal). **Gyula Eres:** Conceptualization (equal); Data curation (equal); Formal analysis (equal); Investigation (equal); Methodology (equal); Resources (equal); Writing – review & editing (equal). **Xinwei Wang:** Conceptualization (equal); Data curation (equal); Formal analysis (equal); Funding acquisition (equal); Investigation (equal); Methodology (equal); Project administration (equal); Resources (equal); Supervision (equal); Writing – review & editing (equal).

DATA AVAILABILITY

The data that support the findings of this study are available from the corresponding authors upon reasonable request.

REFERENCES

[1]S. Chen, L. Qiu, and H.-M. Cheng, "Carbon-based fibers for advanced electrochemical energy storage devices," Chem. Rev. **120**(5), 2811–2878 (2020).
[2]S.-C. Sun, Y. Xu, J.-L. Wen, T.-Q. Yuan, and R. Sun, "Recent advances of lignin-based carbon fibers (LCFs): Precursors, fabrications, properties, and applications," Green Chem. **24**, 5709–5738 (2022).
[3]S. Yang, Y. Cheng, X. Xiao, and H. Pang, "Development and application of carbon fiber in batteries," Chem. Eng. J. **384**, 123294 (2020).
[4]G. Yang, M. Park, and S.-J. Park, "Recent progresses of fabrication and characterization of fibers-reinforced composites: A review," Compos. Commun. **14**, 34–42 (2019).
[5]A. Babapoor, M. Azizi, and G. Karimi, "Thermal management of a Li-ion battery using carbon fiber-PCM composites," Appl. Therm. Eng. **82**, 281–290 (2015).
[6]M. Li and B. Mu, "Effect of different dimensional carbon materials on the properties and application of phase change materials: A review," Appl. Energy **242**, 695–715 (2019).
[7]L. Yang, X. Jin, Y. Zhang, and K. Du, "Recent development on heat transfer and various applications of phase-change materials," J. Clean. Prod. **287**, 124432 (2021).
[8]Z. Ali, Y. Gao, B. Tang, X. Wu, Y. Wang, M. Li, X. Hou, L. Li, N. Jiang, and J. Yu, "Preparation, properties and mechanisms of carbon fiber/polymer composites for thermal management applications," Polymers **13**(1), 169 (2021).

[9]M. Haghgoo, R. Ansari, and M. K. Hassanzadeh-Aghdam, "Prediction of electrical conductivity of carbon fiber-carbon nanotube-reinforced polymer hybrid composites," Composites, Part B **167**, 728–735 (2019).
[10]J. Liu, W. Qu, Y. Xie, B. Zhu, T. Wang, X. Bai, and X. Wang, "Thermal conductivity and annealing effect on structure of lignin-based microscale carbon fibers," Carbon **121**, 35–47 (2017).
[11]J. Liu, T. Wang, S. Xu, P. Yuan, X. Xu, and X. Wang, "Thermal conductivity of giant mono- to few-layered CVD graphene supported on an organic substrate," Nanoscale **8**(19), 10298–10309 (2016).
[12]Y. Xie, Z. Xu, S. Xu, Z. Cheng, N. Hashemi, C. Deng, and X. Wang, "The defect level and ideal thermal conductivity of graphene uncovered by residual thermal reffusivity at the 0 K limit," Nanoscale **7**(22), 10101–10110 (2015).
[13]Y. Xie, P. Yuan, T. Wang, N. Hashemi, and X. Wang, "Switch on the high thermal conductivity of graphene paper," Nanoscale **8**(40), 17581–17597 (2016).
[14]E. López-Honorato, C. Chiritescu, P. Xiao, D. G. Cahill, G. Marsh, and T. J. Abram, "Thermal conductivity mapping of pyrolytic carbon and silicon carbide coatings on simulated fuel particles by time-domain thermoreflectance," J. Nucl. Mater. **378**(1), 35–39 (2008).
[15]Y. Hu, L. Zeng, A. J. Minnich, M. S. Dresselhaus, and G. Chen, "Spectral mapping of thermal conductivity through nanoscale ballistic transport," Nat. Nanotechnol. **10**(8), 701–706 (2015).
[16]E. K. Pek, J. Brethauer, and D. G. Cahill, "High spatial resolution thermal conductivity mapping of SiC/SiC composites," J. Nucl. Mater. **542**, 152519 (2020).
[17]T. Reddyhoff, A. Schmidt, and H. Spikes, "Thermal conductivity and flash temperature," Tribol. Lett. **67**(1), 1–9 (2019).
[18]J. Goeckeritz, G. Aden, and A. Chand, "Nanometer thermal conductivity mapping using laser-based scanning thermal microscopy," Mater. Res. Soc. Symp. Proc. **1754**(1), 81–86 (2015).
[19]A. Laraoui, H. Aycock-Rizzo, Y. Gao, X. Lu, E. Riedo, and C. A. Meriles, "Imaging thermal conductivity with nanoscale resolution using a scanning spin probe," Nat. Commun. **6**(1), 1–8 (2015).
[20]D. M. A. Mackenzie, P. R. Whelan, P. Bøggild, P. U. Jepsen, A. Redo-Sanchez, D. Etayo, N. Fabricius, and D. H. Petersen, "Quality assessment of terahertz time-domain spectroscopy transmission and reflection modes for graphene conductivity mapping," Opt. Express **26**(7), 9220–9229 (2018).
[21]P. Bøggild, D. M. A. Mackenzie, P. R. Whelan, D. H. Petersen, J. D. Buron, A. Zurutuza, J. Gallop, L. Hao, and P. U. Jepsen, "Mapping the electrical properties of large-area graphene," 2D Mater. **4**(4), 042003 (2017).
[22]J. D. Buron, D. H. Petersen, P. Bøggild, D. G. Cooke, M. Hilke, J. Sun, E. Whiteway, P. F. Nielsen, O. Hansen, A. Yurgens, and P. U. Jepsen, "Graphene conductance uniformity mapping," Nano Lett. **12**(10), 5074–5081 (2012).
[23]A. Cultrera, D. Serazio, A. Zurutuza, A. Centeno, O. Txoperena, D. Etayo, A. Cordon, A. Redo-Sanchez, I. Arnedo, M. Ortolano, and L. Callegaro, "Mapping the conductivity of graphene with electrical resistance tomography," Sci. Rep. **9**(1), 1–9 (2019).
[24]A. Cultrera and L. Callegaro, "Electrical resistance tomography of conductive thin films," IEEE Trans. Instrum. Meas. **65**(9), 2101–2107 (2016).
[25]A. K. Khambampati, S. A. Rahman, S. K. Sharma, W. Y. Kim, and K. Y. Kim, "Imaging conductivity changes in monolayer graphene using electrical impedance tomography," Micromachines **11**(12), 1074 (2020).
[26]T.-C. Hou, K. J. Loh, and J. P. Lynch, "Spatial conductivity mapping of carbon nanotube composite thin films by electrical impedance tomography for sensing applications," Nanotechnology **18**(31), 315501 (2007).
[27]S. Xu, H. Zobeiri, N. Hunter, H. Zhang, G. Eres, and X. Wang, "Photocurrent in carbon nanotube bundle: Graded Seebeck coefficient phenomenon," Nano Energy **86**, 106054 (2021).
[28]A. Karamati, N. Hunter, H. Lin, H. Zobeiri, S. Xu, and X. Wang, "Strong linearity and effect of laser heating location in transient photo/electrothermal characterization of micro/nanoscale wires," Int. J. Heat Mass Transf. **198**, 123393 (2022).
[29]T. Wang, X. Wang, J. Guo, Z. Luo, and K. Cen, "Characterization of thermal diffusivity of micro/nanoscale wires by transient photo-electro-thermal technique," Appl. Phys. A **87**(4), 599–605 (2007).
[30]W. Qu, Y. Xue, Y. Gao, M. Rover, and X. Bai, "Repolymerization of pyrolytic lignin for producing carbon fiber with improved properties," Biomass Bioenergy **95**, 19–26 (2016).
[31]C. Deng, T. Cong, Y. Xie, R. Wang, T. Wang, L. Pan, and X. Wang, "*In situ* investigation of annealing effect on thermophysical properties of single carbon nanocoil," Int. J. Heat Mass Transf. **151**, 119416 (2020).
[32]J. Guo, X. Wang, and T. Wang, "Thermal characterization of microscale conductive and nonconductive wires using transient electrothermal technique," J. Appl. Phys. **101**(6), 063537 (2007).
[33]B. Zhu, J. Liu, T. Wang, M. Han, S. Valloppilly, S. Xu, and X. Wang, "Novel polyethylene fibers of very high thermal conductivity enabled by amorphous restructuring," ACS Omega **2**(7), 3931–3944 (2017).
[34]J. Liu, T. Wang, S. Xu, P. Yuan, X. Xu, and X. Wang, "Thermal conductivity of giant mono-to few-layered CVD graphene supported on an organic substrate," Nanoscale **8**(19), 10298–10309 (2016).
[35]B. Zhu, R. Wang, S. Harrison, K. Williams, R. Goduguchinta, J. Schneiter, J. Pegna, E. Vaaler, and X. Wang, "Thermal conductivity of SiC microwires: Effect of temperature and structural domain size uncovered by 0 K limit phonon scattering," Ceram. Int. **44**(10), 11218–11224 (2018).
[36]Y. Xie, B. Zhu, J. Liu, Z. Xu, and X. Wang, "Thermal reffusivity: Uncovering phonon behavior, structural defects, and domain size," Front. Energy **12**(1), 143–157 (2018).
[37]N. Hunter, A. Karamati, Y. Xie, H. Lin, and X. Wang, "Laser photoreduction of graphene aerogel microfibers: Dynamic electrical and thermal behaviors," ChemPhysChem **23**, e202200417 (2022).
[38]Q. Alahmad, M. Rahbar, A. Karamati, J. Bai, and X. Wang, "3D strongly anisotropic intrinsic thermal conductivity of polypropylene separator," J. Power Sources **580**, 233377 (2023).
[39]Y. Xie, T. Wang, B. Zhu, C. Yan, P. Zhang, X. Wang, and G. Eres, "19-Fold thermal conductivity increase of carbon nanotube bundles toward high-end thermal design applications," Carbon **139**, 445–458 (2018).
[40]H. Lin, S. Xu, X. Wang, and N. Mei, "Significantly reduced thermal diffusivity of free-standing two-layer graphene in graphene foam," Nanotechnology **24**(41), 415706 (2013).
[41]J. Gao, D. Xie, X. Wang, X. Zhang, and Y. Yue, "High thermal conductivity of free-standing skeleton in graphene foam," Appl. Phys. Lett. **117**(25), 251901 (2020).
[42]R. Wang, H. Zobeiri, H. Lin, W. Qu, X. Bai, C. Deng, and X. Wang, "Anisotropic thermal conductivities and structure in lignin-based microscale carbon fibers," Carbon **147**, 58–69 (2019).
[43]L. P. Pitaevskii and E. Lifshitz, *Physical Kinetics: Volume 10* (Butterworth-Heinemann, 2012).
[44]E. Tsymbal, *Dielectric Properties of Insulators, PHYSICS 927: Introduction to Solid-State Physics* (University of Nebraska, Lincoln, 2007).
[45]Y. Xie, H. Zobeiri, L. Xiang, G. Eres, J. Wang, and X. Wang, "Dual-pace transient heat conduction in vertically aligned carbon nanotube arrays induced by structure separation," Nano Energy **90**, 106516 (2021).